from weathered ash is precluded by a strong inverse relation ($r^2 = 0.63$, $n = 184$) between BSi and Ti (i.e., BSi dilutes Ti-bearing aluminosilicates). Furthermore, microscopic examination of the sediments reveals an abundance of diatoms and only an occasional volcanic glass shard, except in the two distinct tephra layers. The Nb-enriched volcaniclastic debris, in fact, is primarily weathered residue of volcanic ash, not unweathered glass shards. The observed variability in BSi is thus not a result of enhanced preservation brought on by the presence of volcanic ash.

12. D. A. Harkin, *Tanagnyika Notes* **40**, 20 (1955).
13. The volcaniclastic material also could have been transported to the lake basin by rivers. However, this mechanism is not consistent with the fact that the lake level was low (i.e., the climate was relatively dry) during the time of high Nb/Ti ratio in the sediments. Also, there are no major ash layers in the Pleistocene sections of these cores, whereas there are two in the Holocene sections where, on average, the Nb/Ti ratio in the sediments is lower than that in the Pleistocene. In addition, water transport of volcaniclastic material to the northern basin would not necessarily result in higher diatom burial there. Silica is recycled through several generations of diatoms in a large lake before it is buried in the underlying sediment (*7*, *19*) and in the process will be well mixed throughout the entire lake. A point source of dissolved silica in the north basin would not affect diatom production and burial there as effectively as would upwelling associated with north winds.
14. Differences between the biogenic silica and phosphorus records are not surprising. Changes in soil development associated with varying climate or volcanic sources of P and BSi will influence the nutrient source function to the lake (*20*, *21*). Furthermore, the lake's internal phosphorus cycle is likely to be tightly coupled to the redox behavior of iron, especially where the chemocline, marking the boundary between oxic and anoxic waters, intersects the lake floor. The chemocline is presently at about a 200-m depth in Lake Malawi, but it has migrated vertically by more than 100 m during the Holocene (*22*, *23*). This dynamic behavior of the chemocline very likely affects the geochemical mass balance of phosphorus in Lake Malawi in ways that will affect its delivery to sediments in the deep, anoxic basins offshore.
15. T. C. Johnson, S. L. Barry, Y. Chan, P. Wilkinson, *Geology* **29**, 83 (2001).
16. S. A. Nicholson, in *Environmental Change and Response in East African Lakes*, J. T. Lehman, Ed. (Kluwer Academic, Dordrecht, Netherlands, 1998), pp. 207–232.
17. S. E. Nicholson, in *The Limnology, Climatology, and Paleoclimatology of the East African Lakes*, T. C. Johnson, E. O. Odada, Eds. (Gordon and Breach, Toronto, 1996), pp. 25–56.
18. Climate Variability and Predictability (CLIVAR) Project, *Climate Research for Africa: WCRP No. 16/1999* (World Climate Research Program, 1999).
19. T. C. Johnson, S. J. Eisenreich, *Geochim. Cosmochim. Acta* **43**, 77 (1979).
20. O. A. Chadwick, L. A. Derry, P. M. Vitousek, B. J. Huebert, L. O. Hedin, *Nature* **397**, 491 (1999).
21. G. M. Filipelli, C. Souch, *Geology* **27**, 171 (1999).
22. E. T. Brown, L. Le Callonnec, C. R. German, *Geochim. Cosmochim. Acta* **64**, 3515 (2000).
23. B. P. Finney, T. C. Johnson, *Palaeogeogr. Palaeoclimatol. Palaeoecol.* **85,** 351 (1991).
24. D. J. DeMaster, thesis, Yale University (1979).
25. K. I. Aspila, H. Agemian, A. S. Y. Chau, *Analyst* **101**, 187 (1976).
26. M. Stuiver, P. J. Reimer, *Radiocarbon* **35**, 215 (1993).
27. We thank the government of Malawi for access to Lake Malawi and logistical support for our work in the field; the SADC/GEF Lake Malawi/Nyasa Biodiversity Conservation Project at Senga Bay for housing, laboratory facilities, and ship time aboard the R/V *Usipa*, under the able command of M. Day; M. Talbot for comments on an earlier draft of this manuscript and, along with M. Fillipi, for assistance in the field. Y. Chan, S. Grosshuesch, and J. Agnich contributed substantially in the laboratory. This material is based on work supported by the NSF under grant no. ATM-9709291. This is publication no. 131 of IDEAL.

22 January 2002; accepted 20 February 2002

Asteroid 1950 DA's Encounter with Earth in 2880: Physical Limits of Collision Probability Prediction

J. D. Giorgini,[1] * S. J. Ostro,[1] L. A. M. Benner,[1] P. W. Chodas,[1] S. R. Chesley,[1] R. S. Hudson,[2] M. C. Nolan,[3] A. R. Klemola,[4] E. M. Standish,[1] R. F. Jurgens,[1] R. Rose,[1] A. B. Chamberlin,[1] D. K. Yeomans,[1] J.-L. Margot[5]

Integration of the orbit of asteroid (29075) 1950 DA, which is based on radar and optical measurements spanning 51 years, reveals a 20-minute interval in March 2880 when there could be a nonnegligible probability of the 1-kilometer object colliding with Earth. Trajectory knowledge remains accurate until then because of extensive astrometric data, an inclined orbit geometry that reduces in-plane perturbations, and an orbit uncertainty space modulated by gravitational resonance. The approach distance uncertainty in 2880 is determined primarily by uncertainty in the accelerations arising from thermal re-radiation of solar energy absorbed by the asteroid. Those accelerations depend on the spin axis, composition, and surface properties of the asteroid, so that refining the collision probability may require direct inspection by a spacecraft.

Useful predictions of asteroid encounters with planets, in which the statistical uncertainty in the time of closest approach is ±10 days or less, are generally limited to an interval within a few decades of the time spanned by positional measurements (astrometry), unless optical astrometry spans several years or high-precision delay-Doppler radar measurements are available. This is because long-term solar system dynamics can be a highly nonlinear prediction problem, and measurement error propagation increases the positional uncertainties of an asteroid with time. Here we consider the trajectory of asteroid 1950 DA over a much longer time period and estimate the probability of an Earth encounter.

The possibility of a close approach to Earth was initially recognized in the course of a recent radar experiment that used dynamical force propagation methods that have been used successfully for previous, comparatively short-term predictions of asteroid orbits. Then, because of the quality and extent of the orbit measurements, we examined several factors that are normally neglected in asteroid trajectory prediction and hazard studies so as to more accurately characterize trajectory knowledge and confirm the initial impact probability calculation. These factors include computational noise, galactic tides, perturbations due to the gravitational encounters of the asteroid with thousands of other asteroids, an oblate Sun whose mass is decreasing, the role of planetary mass uncertainties, acceleration due to solar wind and radiation pressure acting on the asteroid, and the acceleration of the asteroid due to thermal emission of absorbed solar energy.

Asteroid (29075) 1950 DA was discovered on 23 February 1950 (*1*). It was observed for 17 days and then lost until an object discovered on 31 December 2000 and designated 2000 YK66 (*2*) was recognized just 2 hours later as being the long-lost 1950 DA (*3*). We conducted delay-Doppler radar observations using methods described by Ostro (*4*) at Goldstone and Arecibo on 3 to 7 March 2001, during the asteroid's 7.79×10^6 km approach to Earth (a distance 20.3 times larger than that separating Earth and the Moon). Our echoes (Fig. 1) reveal a slightly asymmetrical spheroid with a mean diameter of 1.1 km.

Our first radar observations, at Goldstone, corrected the initial orbit prediction by -35 ± 35 mm s^{-1} in radial velocity and $+7.9 \pm 0.9$ km in range (*5*). We incorporated this radar astrometry in a weighted least-squares orbit estimation for a 10 March 2001 epoch (*6*). Then, to determine the time interval over which approaches to planetary bodies could be accurately predicted, we mapped the known orbit uncertainties at the solution epoch (contained in the measurement covariance matrix) to other times by numerically integrating the equations

[1]Jet Propulsion Laboratory, California Institute of Technology, Pasadena, CA 91109–8099, USA. [2]School of Electrical Engineering and Computer Science, Washington State University, Pullman, WA 99164–2752, USA. [3]Arecibo Observatory, Arecibo, Puerto Rico 00612, USA. [4]Lick Observatory, University of California, Santa Cruz, CA 95064, USA. [5]California Institute of Technology, Pasadena, CA 91125, USA.

*To whom correspondence should be addressed. E-mail: Jon.Giorgini@jpl.nasa.gov

of motion for the best-fit trajectory along with the linearized variational partial derivatives of that trajectory (*7*). The resulting linearized Earth impact probability was 0.0033 (0.33%) on 16 March 2880 (Table 1). This is three orders of magnitude higher than the impact probability calculated for any other object large enough to penetrate Earth's atmosphere and corresponds to a hazard rating of +0.17 on the Palermo Technical Scale, or 1.5 times greater than the background risk through 2880 (*8*). The rest of this discussion is based on orbit solution number 37 (Table 2), which is our best fit to an extended astrometric data set (*9–14*).

Linearized covariance matrix mappings neglect higher-order terms in the partial derivative equations and can result in significant errors over time because of nonlinearities in the actual orbital motion of the asteroid. Therefore, to evaluate the validity of our linearized method, we performed a Monte Carlo study. We sampled the six-dimensional uncertainty region at the solution epoch by constructing a Gaussian probability distribution of points around the nominal position and velocity vector (*15*). We randomly selected 10,000 statistically possible starting points and integrated each one of these "virtual asteroids" to 2880 using the complete nonlinear equations of motion. The distribution of statistically possible trajectories after 879 years closely duplicated the prediction of our linearized method (Fig. 2).

The Monte Carlo study also revealed that the orbit uncertainty region is gravitationally modulated, expanding and contracting several times along the direction of motion as time passes rather than increasing secularly on average, as is normally the case (*16*). Virtual asteroids that lead the nominal position get pulled back, while those behind get pulled forward. This phenomenon appears to be caused by gravitational accelerations in the direction of motion that increase the orbital energy (and hence the semimajor axis) of the asteroid, which decreases the average orbital angular velocity. The outcome is a gradual displacement of the virtual asteroid backward in the uncertainty space, whereupon the process reverses direction. Thus, particles in the uncertainty region remain in a bounded oscillation centered on the nominal position and oriented along the direction of orbital motion. This fluctuation in the uncertainty space may be the manifestation of the combination of a Geographos-type mean motion resonance (*17*) and a resonant restoring force (*18*), in which the observed oscillation in orbital uncertainty growth is due to Earth's gravity acting on the heliocentric mean longitude of 1950 DA (Fig. 3).

All calculations for the reference trajectory described above included gravitational and relativistic point-mass effects on the asteroid by the Sun, planets, Moon, and the three large asteroids Ceres, Pallas, and Vesta (*19*), which comprise about 60% of the mass of the main asteroid belt. For 1950 DA, we have examined the contribution to the uncertainty space from several additional sources that could potentially be significant over such a long period of time (*20*). These include numerical integration error, galactic tides, asteroid gravitational

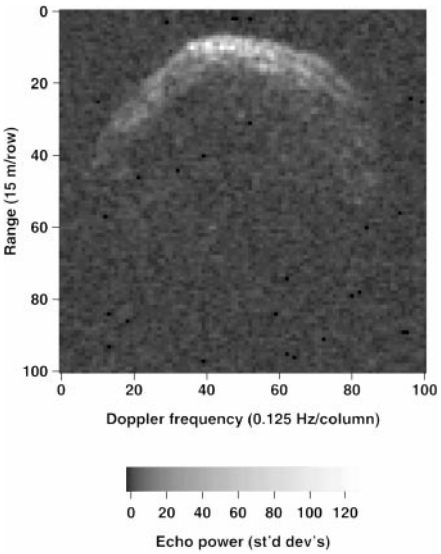

Fig. 1. Arecibo (2380 MHz, 13 cm) delay-Doppler echo-power image of 1950 DA on 4 March 2001, from a distance of 0.052 AU (22 lunar distances). Vertical resolution is 15 m, and horizontal resolution is 0.125 Hz (7.9 mm s^{-1} in radial velocity).

Table 1. 1950 DA planetary close approaches less than 0.1 AU from discovery to 2880. One AU is 149,597,870.691 km. CA dist. is the highest probability approach distance of the reference trajectory. Min dist. and Max dist. are the minimum and maximum 3σ distances from the body at the nominal close approach time. V_{rel} is the relative velocity, TCA3Sg is the 3σ uncertainty in the time of nominal close approach, and P_i is the linearized probability of impact (the fraction of the uncertainty region overlapping the projected area of the Earth).

Date			Body	CA dist. (AU)	Min dist. (AU)	Max dist. (AU)	V_{rel} (km s^{-1})	TCA3Sg (min)	P_i
1950	Mar	12.983	Earth	0.059286	0.059286	0.059287	12.973	0.12	0.000000
2001	Mar	5.058	Earth	0.052073	0.052073	0.052073	14.732	0.00	0.000000
2032	Mar	2.281	Earth	0.075751	0.075750	0.075751	15.580	0.07	0.000000
2074	Mar	19.930	Earth	0.095461	0.095461	0.095461	12.090	0.02	0.000000
2105	Mar	10.069	Earth	0.036316	0.036316	0.036316	13.803	0.09	0.000000
2136	Mar	11.864	Earth	0.042599	0.042596	0.042602	13.355	0.83	0.000000
2187	Mar	8.967	Earth	0.035214	0.035206	0.035222	14.298	2.81	0.000000
2218	Mar	20.452	Earth	0.084991	0.084877	0.085105	12.241	26.9	0.000000
2373	Mar	18.008	Earth	0.059030	0.058999	0.059061	12.729	6.08	0.000000
2455	Mar	6.304	Earth	0.087684	0.087665	0.087702	16.288	1.86	0.000000
2539	Sep	1.736	Mars	0.082053	0.082041	0.082065	14.275	1.74	0.000000
2639	May	11.52	Mars	0.070470	0.070464	0.070476	14.537	1.59	0.000000
2641	Mar	14.330	Earth	0.015634	0.015604	0.015663	14.339	5.65	0.000000
2736	Mar	20.928	Earth	0.048456	0.048125	0.048787	12.895	51.95	0.000000
2809	Mar	19.957	Earth	0.033387	0.032627	0.034149	13.238	108.1	0.000000
2840	Aug	15.066	Mars	0.077116	0.072918	0.081508	15.805	335.4	0.000000
2860	Mar	20.283	Earth	0.036918	0.028721	0.045247	13.138	1176	0.000000
2880	Mar	16.570	Moon	0.002454	0.001048	0.043553	14.229	4166	0.000000
2880	Mar	16.836	Earth	0.001954	0.000000	0.040600	14.246	4735	0.003266

Table 2. 1950 DA orbit solution number 37 with estimated formal uncertainties at the solution epoch 10.0 March 2001 (coordinate time). The optical data post-fit residual mean and root mean square (rms) are (0.103, 0.517) arc seconds. The normalized rms (n-rms), obtained by first dividing each measurement by its assigned uncertainty, is 0.636. For radar delay, the residual mean and rms are (−0.030, 1.571) microseconds and n-rms is 0.761. Doppler residual mean and rms are (−0.027. 0.5164) Hz and n-rms is 1.012. The combined data-type residual n-rms is 0.648. Elements are in the ICRF93/J2000 coordinate frame of the DE-405 JPL planetary ephemeris, a quasar-based radio frame, generally within 0.01 arc seconds of the optical FK5/J2000 frame. Angular elements are referred to the ecliptic and mean equinox of J2000.

Osculating element	Value	Post-fit SD (1σ)	
Eccentricity	0.5078302902	+/−0.0000000425	
Perihelion distance	0.8365252752	+/−0.0000000722	AU
Time of perihelion	2452012.4280994495	+/−0.0000060846	Julian day number
Longitude of ascending node	356.8249761034	+/−0.0000076068	deg
Argument of perihelion	224.5056599305	+/−0.0000096032	deg
Inclination	12.1839903721	+/−0.0000056526	deg
Semimajor axis	1.6996683430	+/−0.0000000009	AU
Orbital period	809.36553169	+/−0.00000064	days

perturbations, loss of solar mass, solar wind, solar oblateness and radiation pressure, uncertainties in planetary masses, and accelerations due to the time-delayed anisotropic thermal re-radiation of incident solar radiation, also known as the Yarkovsky effect (*21*). Each of these factors primarily alters the along-track position of 1950 DA, either advancing or delaying the arrival of the object at the intersection with the orbit of Earth in 2880. Deviations in the cross-track and normal directions were two to five orders of magnitude smaller than along the direction of motion. The influence of these factors on the predicted along-track position of 1950 DA are summarized in Table 3 and Figs. 3 and 4.

Numerical integration error can accumulate through rounding or truncation caused by machine precision limits, especially near planetary close approaches when the time-step size must change rapidly. We found that the cumulative relative integration error for 1950 DA remains less than 1 km until 2105, thereafter oscillating around zero with a maximum amplitude of 200 km until the 2809 Earth encounter (*22*). It then grows to –9900 km at the 2880 encounter, changing the nominal time of close approach on 16 March 2880 by –12 min.

To identify asteroids other than Ceres, Pallas, and Vesta whose gravity might affect the motion of 1950 DA, we numerically integrated the orbits of 7196 numbered asteroids having diameters greater than 10 km over the next 880 years. We identified 28,199 approaches to 1950 DA, computed the trajectory deflection angles due to each gravitational encounter, and then linearly extended the deflection to 2880. For the 2051 asteroids found to have one or more encounters with 1950 DA, the sum of these deflections provided a perturbing index number (PIN) that summarized the cumulative deflection of each object (*23*). The equations of motion were then extended to include the 61 perturbers having the largest PINs, which accounted for 80% of the perturbation caused by all 2051 objects (*24*). This changed the along-track position by –1.2 days after 879 years.

The shape of the Sun deviates slightly from that of a sphere, resulting in a nonuniform gravitational potential field. We incorporated the acceleration caused by this solar oblateness using a J2 zonal harmonic in the range 2.0×10^{-7} to 1.6×10^{-7}. This alters the arrival time at the 2880 orbit intersection by between +49 and +21 min.

We considered solar particle-wind and radiation pressure (SRP) acting on a sphere 1 km in diameter, with a constant solar luminosity at 1 astronomical unit (AU) of 1367 watts m^{-2}, a bulk density of 3 g cm^{-3} (the minimum value consistent with the measured spin rate of 1950 DA, assuming no tensile strength) (*25*, *26*), and a uniform optical albedo of 0.25 (*27*). The resulting acceleration changed the arrival time at the 2880 intersection by –9.1 days (*28*).

Planetary masses and positions are estimated quantities with their own statistical uncertainties (*29*). We examined the effect of such uncertainties by biasing all planetary masses by ±3 SD (3σ) for the reference case. After 879 years, the +3σ and –3σ cases altered the intersection arrival date by +1.1 days and –1.3 days, respectively.

The direction of the rotational axis of 1950 DA plays a major role in determining the small accelerations acting on the asteroid because of the Yarkovsky effect, but our shape solutions for 1950 DA only constrain its location to lie within 30° to 50° of two equally possible poles. This is due in part to the small sky angle spanned by useful radar observations. In the J2000.0 ecliptic longitude and latitude (λ, β) coordinate system, defined with respect to Earth's heliocentric orbital plane on 1 January 2000 at 12:00 (coordinate time), these possible poles are (97°, 79°) and (18°, –40°). We varied the unknown surface thermal conductivity (assumed to be uniformly distributed over a sphere) by two orders of magnitude, from 0.01 to 1.0 W mK^{-1} for both pole solutions, and numerically integrated the force models over 879 years. For the first pole, a case of direct rotation, the nominal time of arrival at the orbit intersection varied from +9.6 to +4.7 days.

For the second pole solution (retrograde rotation), arrival at the intersection varied from –57.3 to –16.5 days. Thus, for the direct case (anticlockwise spin as seen from the north celestial pole), thermal radiation acceleration tends to counter the other perturbations acting on the asteroid, moving the uncertainty region closer to Earth. Our retrograde pole solution

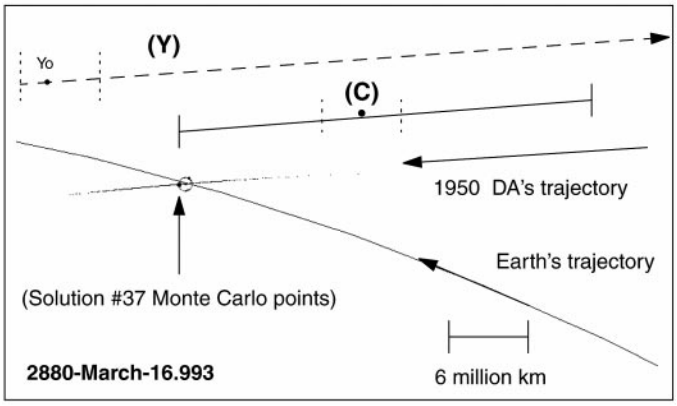

Fig. 2. 500-point Monte Carlo region seen from north of the ecliptic plane when Earth passes through the descending orbit track of 1950 DA on 16 March 2880. Curve C, which is offset from the actual trajectory of the asteroid in the cross-track direction for clarity, depicts the range of statistically possible asteroid positions that result when all perturbations except the unknown Yarkovksy effect are combined in a single numerical integration. The vertical bars on either side of the nominal point C depict the Monte Carlo region along-track shift for ±3σ planetary masses. Line Y, also offset from the trajectory of 1950 DA and extending off-diagram to the right, depicts the range of positions due to the Yarkovsky effect only, obtained by varying surface thermal conductivity (0.01 to 1.0 W mK^{-1}) for both of our possible pole solutions. Vertical lines on Y denote the extent of variation found due to the surface thermal conductivity for the case of our (97°, 79°) direct pole rotation solution only, with Y_0 marking the case of 0.1 W mK^{-1}. A bulk density of 3 g cm^{-3} is assumed. This illustrates how Yarkovksy accelerations could potentially act to counter the other perturbations by advancing the 1950 DA trajectory region forward on its orbit track.

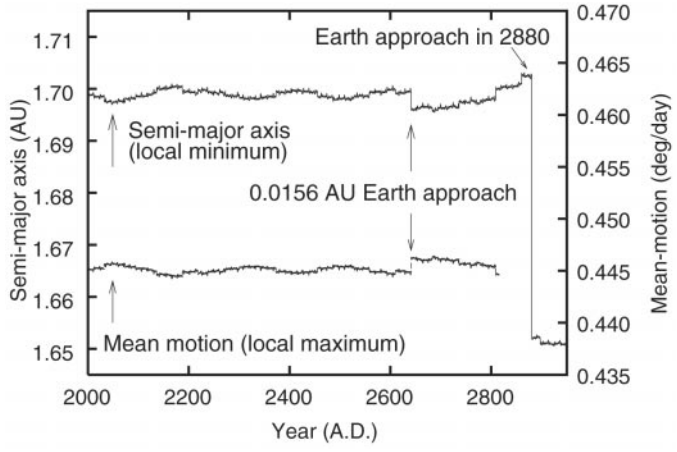

Fig. 3. Variation in 1950 DA's semimajor axis (left scale) and mean motion (that is, the average orbital angular velocity, shown on the right-hand scale) from 2001 to 2880. Planetary close approaches appear as vertical discontinuities. The effect of the resonance controlling the uncertainty region growth, most evident in Monte Carlo simulations, is visible here in the oscillations of the semimajor axis and mean motion. The mean motion trend is terminated in 2810 for plot clarity.

(clockwise spin) moves the uncertainty region further away, probably eliminating the possibility of a collisional outcome. Only a very small portion of the Yarkovsky parameter space has been examined.

The additional error sources considered here primarily advance or delay the arrival time of 1950 DA at the intersection with the orbit of Earth. Their effect remains cumulatively small until about 20 years before the 2880 encounter. Close approaches to Earth in 2809 and 2860 gravitationally amplify the uncertainty space at "the last minute," limiting what can be concluded about the possibility of Earth impact in 2880 (Fig. 4). A close Earth encounter would then disrupt the uncertainty space in such a way that accurate trajectory predictions beyond that date could not be made. Although the orbital paths of Earth and 1950 DA permit a 20-min window of intersection on 16 March 2880, the location of the asteroid along its orbit depends on physical parameters that have not yet been well determined. These include its mass, axis of rotation, specular and diffuse optical reflectivity, thermal conductivity, and regolith depth. If the spin axis of 1950 DA is fixed near our direct rotation pole solution, solar pressure and asteroid perturbations could counter the Yarkovsky effect so that the probability of a collision in 2880 would be comparable to that of the initial detection case of 0.33%. Thus, the impact probability currently lies in the interval from 0 to 0.33%, where the upper bound will increase or decrease more rapidly as physical knowledge improves than as ground-based optical astrometry accumulates. We are unable to calculate a reliable, specific collision probability, because the trajectory uncertainties are dominated by unmeasured or poorly determined systematic physical effects.

That 1950 DA has one of the best-determined asteroid (or comet) orbit solutions is due to the combination of an orbit moderately inclined to the ecliptic plane (reducing in-plane perturbations), high-precision radar astrometry, a 51-year optical data arc, and an uncertainty region controlled by resonance. 1950 DA is the only known asteroid whose predicted impact potential depends primarily on its physical properties, not on positional measurement uncertainties. It is also the only recognized case in which gravitational resonance controls the orbital uncertainty growth before a possibly very close planetary encounter.

The next radar opportunity for this asteroid is in 2032. The cumulative effect of Yarkovsky acceleration since 2001 might be detected with radar measurements obtained then, but this would be more likely during radar opportunities in 2074 or 2105. Earlier Yarkovsky detection or orbital uncertainty reduction might be possible with space-based optical astrometric systems. Ground-based photometric observations might better determine the pole direction of 1950 DA much sooner. Depending on the results of such experiments, a satisfactory assessment of the collision probability of 1950 DA may require direct physical analysis with a spacecraft mission.

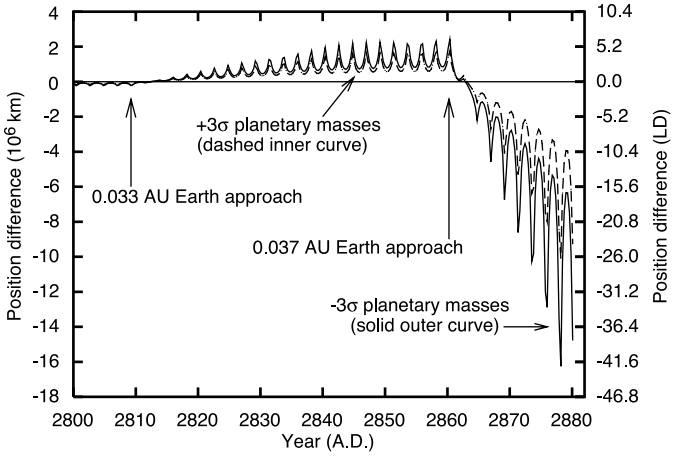

Fig. 4. Along-track deviations from the 1950 DA solution number 37 reference trajectory when all additional perturbations except the unknown Yarkovsky acceleration are combined in a single numerical integration, for both $\pm 3\sigma$ planetary mass cases. 1 lunar distance (LD) is 384,400 km. The perturbations remain cumulatively small for 800 years; by the time of the 2809 Earth encounter, the along-track change is $-58{,}000$ km (-67 min), only two times the linearly mapped formal covariance 1σ uncertainty for that time. These slightly altered approach circumstances cause the perturbed trajectory to deviate even more rapidly thereafter and then again to an even greater extent after the 2860 Earth encounter.

Table 3. Trajectory propagation factors and their individual and combined effect on our prediction of the along-track position of 1950 DA, on 16.0 March 2880, just before the time of nominal orbit intersection with Earth. Differences are expressed relative to the reference trajectory. Bracketed quantities indicate the bounding value found by varying the parameter over the intervals described in the text.

Trajectory propagation factor	Along-track effect	
	Distance (km)	Time
(A) Galactic tide	-8400	-10 min
(B) Numerical integration error	-9900	-12 min
(C) Solar mass loss	$+13300$	$+16$ min
(D) Solar oblateness (J2)	$(+42100, +17600)$	$(+49, +21)$ min
(E) 61 additional asteroids	-1.5×10^6	-1.2 days
(F) Planetary mass uncertainty	$(+1.38, -1.54) \times 10^6$	$(+1.1, -1.3)$ days
(G) Solar radiation pressure	-11.2×10^6	-9.1 days
Combined (A-G)	$(-11.0, -17.6) \times 10^6$	$(-9.0, -14.3)$ days
Yarkovsky effect only	$(+11.9, -71.0) \times 10^6$	$(+9.6, -57.7)$ days

References and Notes

1. C. A. Wirtanen, *Minor Planet Circ. 416* (1950).
2. LONEOS Sky Survey, *Minor Planet Electron. Circ. 2001-A22* (2001).
3. C. M. Bardwell, *Minor Planet Electron. Circ. 2001-A26* (2001).
4. S. J. Ostro, in *Encyclopedia of Physical Science and Technology*, ed. 3, vol. 12 (Academic Press, San Diego, CA, 2002), pp. 295–327.
5. Delay-Doppler corrections to the orbit at the start of the radar experiment were atypically small because of the long time interval spanned by preexisting optical astrometry, which consisted of 119 plane-of-sky angular measurements reported by 15 different observing sites spanning 51 years. This optical astrometry and subsequent measurements are available from the Minor Planet Center, Cambridge, MA.
6. C. L. Lawson, R. Hanson, *Solving Least Squares Problems*, SIAM Classics in Applied Mathematics, vol. 15 (Society for Industrial and Applied Mathematics, Philadelphia, PA, 1995); G. J. Bierman, *Factorization Methods for Discrete Sequential Estimation* (Academic Press, New York, 1977).
7. The linearized variational partial derivatives are the elements $\partial \mathbf{x}/\partial \mathbf{x}_0$ of a state-transition matrix $\mathbf{M}$ which relates the asteroid position and velocity (state) vector $\mathbf{x}_0$ at time τ_0 to the state vector $\mathbf{x}$ at another time τ. Given matrix $\mathbf{R}^{-1}$, the upper-triangularized square root of the covariance matrix at epoch τ_0, the mapped covariance at time τ is then $\mathbf{S} = (\mathbf{M}\mathbf{R}^{-1})(\mathbf{M}\mathbf{R}^{-1})^T$.
8. S. R. Chesley, P. W. Chodas, A. Milani, G. B. Valsecchi, D. K. Yeomans, *Icarus*, in press.
9. After completion of the radar experiment, a three-dimensional shape model was estimated from the delay-Doppler data set, thereby locating the center of mass (COM) of 1950 DA. This permitted additional delay-Doppler astrometry with measurement uncertainties 5 to 10 times smaller than those before the shape-model COM solution (typically a 0.3-μs measurement uncertainty after COM solution versus a 1.5- to 3-μs uncertainty before its determination). Two historical optical observations that had not been previously recognized were also identified in images taken in 1981 by S. Tritton as part of the Australia-based UK Schmidt Telescope program. There was evidence of a $+1$ arc second mean bias in some of the original 1950 right-ascension plate measurements, so most of the original plates (those with well-defined image trails of the asteroid) were remeasured in the modern reference frame of the Tycho-2 star catalog, together with additional plates that had not been measured previously. An orbit solution based only on the resulting internally consistent optical data also indicated the possible impact in 2880 that we had seen previously only in solutions

based on combined radar and optical data, in which the high-precision radar astrometry had mitigated the effect of biased optical data. The corrected and extended set of data referred to here includes 145 optical, eight time-delay, and five Doppler measurements. When we included the refined astrometry, the estimated impact probability increased slightly to 0.33%.
10. S. Hudson, *Remote Sens. Rev.* **8**, 195 (1993).
11. Radar astrometry is available from the Jet Propulsion Laboratory (JPL) Solar System Dynamics radar astrometry database (http://ssd.jpl.nasa.gov/radar_data.html) or *Minor Planet Electron. Circ. 2001-O20* (2001).
12. M. Read, A. Boattini, G. Forti, G. D'Abramo, *Minor Planet Electron. Circ. 2001-F44* (2001); see also A. Boattini, G. D'Abramo, G. Forti, R. Gal, *Astron. Astrophys.* **375**, 293 (2001).
13. A. R. Klemola, *Minor Planet Electron. Circ. 2001-K23* (2001).
14. Numerically integrated orbit, ephemeris, error, and close approach analyses are available from the NASA/JPL Horizons On-Line Ephemeris System [J. D. Giorgini *et al.*, *Bull. Am. Astron. Soc.* **28**, 1158 (1996)]: http://ssd.jpl.nasa.gov/horizons.html and telnet://ssd.jpl.nasa.gov:6775.
15. P. W. Chodas, D. K. Yeomans, "Am. Astron. Soc. paper 99-462" (Girdwood, Alaska, 1999).
16. Graphical animations of 500 statistically possible Monte Carlo trajectories, their dynamical distribution over time, resonance modulation, and encounter with Earth in 2880 are available on *Science* Online at www.sciencemag.org/cgi/content/full/296/5565/132/DC1 as animations 1 through 4.
17. A mean motion resonance (or commensurability) occurs when the average orbital angular velocity ratio of two or more objects is very close to a ratio of integers. The objects return to the same relative positions, producing a repetitive, periodic gravitational force.
18. A. Milani, M. Carpino, G. Hahn, A. M. Nobili, *Icarus* **78**, 212 (1989); A. Milani, S. Baccili, *Celestial Mech. Dyn. Astron.* **71**, 35 (1998).
19. T. D. Moyer, *Mathematical Formulation of the Double-Precision Orbit Determination Program (DPODP)* (JPL Technical Report 32-1527, JPL, Pasadena, CA, 1971); E. M. Standish, X X Newhall, J. G. Williams, D. K. Yeomans, in *Explanatory Supplement to the Astronomical Almanac*, P. K. Seidelmann, Ed. (University Science Books, Mill Valley, CA, 1992), pp. 279–323.
20. Some smaller factors examined include the mass of the Sun decreasing at a rate of -5.76×10^9 kg s^{-1} because of luminosity and particle emission [J. R. Jokipii, C. P. Sonnett, S. Giampapa, Eds., *Cosmic Winds and the Heliosphere* (Univ. of Arizona Press, Tucson, AZ, 1989)]. For the case of negligible matter infall, numerical integration shows that this solar mass loss rate causes a +13300-km along-track change in the orbit of 1950 DA by 2880 (a +16-min change in arrival at the intersection with the orbit of Earth). Galactic tidal perturbations [J. Heisler, S. Tremaine, *Icarus* **65**, 13 (1986)] are dominated by the distribution of mass within 300 parsecs of the solar system [K. A. Innanen, *Earth Moon Planets* **72**, 1 (1996)]. Inclusion of this acceleration in a numerical integration reveals a −8400-km along-track change in the orbit of 1950 DA by 2880, producing a −10-min change in the arrival timing. Galactic tidal acceleration ($\sim 10^{-15}$ mm s^{-2}) is three orders of magnitude greater than solar particle wind pressure acceleration at 1 AU but six orders of magnitude less than that of solar radiation pressure. These accelerations, although small, alter 1950 DA planetary encounter circumstances, resulting in a gravitationally amplified effect on the trajectory after 879 years. For comparison, the position of Mars, having no planetary encounters, changes only −85 km as a result of solar mass loss through 2880. With an 80% chance that 1950 DA has dynamically migrated from the inner main belt into its current Earth-crossing orbit (W. F. Bottke, personal communication, 31 May 2001), it is unlikely to experience cometary outgassing accelerations.
21. The Yarkovsky effect has been observed affecting spacecraft motion and is potentially significant for long-term asteroid motion. It is a function of the mass, size, shape, spin state, and global distribution of surface optical and thermal properties of an object. For Yarkovsky calculations, we used the OrbFit Yarkovsky model and software [D. Vokrouhlický, A. Milani, S. R. Chesley, *Icarus* **148**, 118 (2000)].
22. Our integrations are normally performed in 64-bit floating-point arithmetic ("double-precision") using a variable order, variable multistep, Adams-Krogh integrator, with local error tolerances of 10^{-14} and a maximum predictor/corrector order of 14/15. To reveal the cumulative machine numerical error in this approach, we integrated a reference trajectory using much slower but more precise 128-bit arithmetic ("quadruple-precision"), with local error tolerances of 10^{-19} and a maximum 21/22 order predictor/corrector. The quadruple-precision trajectory was then differenced with the double-precision trajectory to assess numerical error in the faster double-precision integrations.
23. An asteroid's PIN = $\Sigma LN\delta$, where L is the orbit perimeter length (9.953328 AU for 1950 DA); $N = (\tau_m - \tau_e)/p$, the map time minus the encounter time, divided by the orbit period (the number of orbits between the encounter and the 2880 map time); and $\delta = 2\tan^{-1}(GM_s v^{-2} d^{-1})$, the deflection angle due to the close approach, where G is the gravitational constant, M_s the mass of the two bodies, v their relative speed, and d the minimum approach distance. The masses of perturbing asteroids were approximated by assuming a bulk density of 3 g cm^{-3}, a diameter (in km) based on the absolute visual magnitude H_v, an albedo (p_v) common for the spectral type of the object, and the relation $\log_{10} p_v = 6.259 - 2\log_{10} D_{eff} - 0.4H_v$ [E. Bowell *et al.*, in *Asteroids II*, R. P. Binzel, T. Gehrels, M. S. Matthews, Eds. (Univ. of Arizona Press, Tucson, AZ, 1989), p. 551].
24. Asteroid 10 Hygiea was the most significant perturber other than Ceres, Pallas, and Vesta. Despite an average approach distance of 1.0 AU, 42 such Hygeia encounters with a mean relative speed of 3.9 km s^{-1} cause 19.8% of the total perturbation detected. This is 2.7 times the total effect of the next biggest perturber, 704 Interamnia. The single greatest perturbation is from a 0.003261-AU approach by 78 Diana on 5 August 2150. Asteroid 4217 Engelhardt approaches 1950 DA most closely, in 2736, at 0.001723 AU (~0.7 lunar distances), but the cumulative perturbative effect by 2880 is negligible.
25. With an optically determined synodic rotation period of 2.1216 ± 0.0001 hours, 1950 DA is one of the fastest known rotators among objects that large. See also *IAU Circular 7735* regarding asteroid 2001 OE84 [P. Pravec, personal communication, 12 August 2001; L. Šarounová, Ondřejov NEO Photometric Program (http://sunkl.asu.cas.cz/~ppravec/neo.htm)].
26. P. Pravec, A. W. Harris, *Icarus* **148**, 12 (2000).
27. This geometric albedo is at the more reflective end of the range common for asteroids, consistent with the diameter from our delay-Doppler shape inversion and the $H_v = 17.0 \pm 0.6$ mean visual magnitude we estimate. Spectral class has not been determined for 1950 DA.
28. The instantaneous acceleration due to solar radiation pressure was modeled as $d^2\mathbf{r}/dt^2 = (C_1 m^{-1} |\mathbf{r}|^{-2})\mathbf{F}$, where $\mathbf{r}$ is the Sun-to-Earth position vector, C_1 is a solar flux constant at 1 AU (2.27545 × 10^{-7} kg AU^3 m^{-2} day^{-2}), m is the mass of the asteroid, and $\mathbf{F}$ is a vector of geometric reflectivities (here, the exposed half-sphere surface area scaled by a reflectivity factor of $1 + p_v$, acting in the radial direction only).
29. The DE-405 planetary ephemeris estimate of Earth mass $M_\oplus$ has a 1σ uncertainty of $6 \times 10^{-8} M_\oplus$ [E. M. Standish, in *Highlights of Astronomy*, I. Appenzeller, Ed. (Kluwer Academic, Dordrecht, Netherlands, 1995), pp. 180–184; also at http://ssd.jpl.nasa.gov/iau-comm4].
30. We are grateful to V. Negrón, A. Hine, and the staff of the Arecibo Observatory, as well as F. Krogh for his valuable insights and suggestions regarding numerical integration. Part of this research was conducted at JPL, California Institute of Technology (Caltech), under contract NASA. The Arecibo Observatory is part of the National Astronomy and Ionosphere Center, which is operated by Cornell University under a cooperative agreement with NSF and with support from NASA. Astrometric plate reduction work was supported by an NSF grant. Some of our Arecibo observations were obtained with the Caltech Baseband Recorder, whose development and fabrication were funded by NSF.

19 November 2001; accepted 27 February 2002

Evidence for the Effect of Learning on Timing of Reproduction in Blue Tits

Fabrizio Grieco,* Arie J. van Noordwijk, Marcel E. Visser

We experimentally show that in blue tits (*Parus caeruleus*) egg-laying date is causally linked to experience in the previous year. Females that received additional food in the nestling period in one year laid eggs later in the next year compared with the control birds, whatever the degree of synchronization with the natural food abundance in the previous year. As a result, they raised their brood much later than the peak period of nestling food availability in the next year. The response to experience is adaptive for blue tits, which live in heterogeneous habitats where the peak period of food varies, but once settled will breed at the same location for life.

In birds, the degree of synchrony of the breeding cycle with the period of maximum food abundance for nestlings is crucial to the condition and survival probability of the offspring (*1*, *2*). Because reproduction starts much earlier than the time of maximum food requirement of the offspring, we expect birds to start reproduction in response to cues that predict the time of maximum food abundance. A number of such cues have been suggested, including day length, temperature, food abundance at the time of egg production, and phenology of the vegetation (*3*–*5*). However, all these studies emphasize the im-

Netherlands Institute of Ecology, Center for Terrestrial Ecology, Post Office Box 40, 6666 ZG Heteren, Netherlands.

*To whom correspondence should be addressed. E-mail: grieco@cto.nioo.knaw.nl